# ARTICLES

## State-Resolved Differential Cross Sections for Crossed-Beam Ar–NO Inelastic Scattering by Direct Ion Imaging

**L. S. Bontuyan, A. G. Suits, and P. L. Houston***

*Department of Chemistry, Cornell University, Ithaca, New York 14853-1301*

**B. J. Whitaker**

*School of Chemistry, Leeds University, Leeds, LS2 9JT United Kingdom*

*Received: January 12, 1993; In Final Form: March 15, 1993*

State-to-state differential cross sections for inelastic collisions of NO with Ar have been measured in a crossed-beam experiment using time-of-flight ion imaging. Rotational rainbow peaks are observed in the angular distributions, and these move to backward scattering angles with increasing final rotational level. The images are analyzed using a Monte Carlo forward convolution program that accounts for the transformation from the center-of-mass differential cross sections to the experimental image. The results are interpreted using a simple two-dimensional hard ellipse model to provide quantitative insight into the anisotropy of the potential energy surface. For NO ($j' = 18.5$), two rainbow peaks are observed. These double rainbows have been predicted for scattering of atoms from heteronuclear molecules, but they have not previously been directly observed in the angular distributions. The analysis is also used to obtain the eccentricity of the hard ellipse potential from the positions of the two rainbow peaks. The angular distributions for the spin–orbit conserving collisions and spin–orbit changing collisions are remarkably similar, even though they were thought to involve two different potential energy surfaces. An alternative mechanism is proposed to account for the spin–orbit changing collisions through non-Born–Oppenheimer coupling of nuclear and electronic motion.

### I. Introduction

Angular distributions from scattering experiments provide a sensitive probe of interparticle interaction potentials. These techniques have been extensively exploited in nuclear physics since the 1930s, but their application to the study of interatomic and intermolecular forces only emerged in the past two decades with the development of crossed molecular beam methods.[1] Atom–atom scattering experiments now provide extremely accurate interatomic potentials for nearly any system of interest.[2] For atom–molecule scattering, however, the additional nuclear degrees of freedom, the anisotropy of the potential, and the possible existence of reactive channels require that the angular distribution be determined for individual quantum states of the products in order to provide detailed insight into the potential energy surface. These state-to-state differential cross sections have thus become ardently sought experimental quantities, and rapid progress has been made, both for inelastic[3-8] and reactive[9,10] scattering.

This report presents the results of a crossed-beam study of rotationally inelastic scattering of NO with Ar, obtained using an extension of the ion-imaging technique originally described by Chandler and Houston.[11] The application of time-of-flight ion imaging to crossed-molecular beam studies results in a powerful and versatile tool; angular distributions are recorded for all angles simultaneously, and the method may be applied to yield state-resolved results wherever resonance-enhanced multiphoton ionization (REMPI) techniques are applicable. A preliminary report of our investigations has already appeared.[12]

Inelastic rotational energy transfer (RET) in open-shell molecules remains an area of considerable theoretical and experimental interest because of the participation of the electronic degrees of freedom in the scattering process.[13-22] The $^2\Pi_{1/2}$ ground electronic state of NO lies approximately 123 $cm^{-1}$ below the $^2\Pi_{3/2}$ spin–orbit excited state, and the rotational levels in each $^2\Pi$ state are also split into two nearly degenerate levels depending upon the direction of nuclear rotation with respect to electronic orbital angular momentum (Λ-type doubling).

For the Ar + NO system, two adiabatic potential energy surfaces are necessary to describe the interaction. One of these, in which the unpaired electron occupies an orbital perpendicular to the plane of the three atoms, is of A″ character in $C_s$ symmetry, while the other, in which the unpaired electron occupies an orbital in the plane of the three atoms, is of A′ character.[23] Alexander showed that in the Hund's case (a) limit the spin–orbit conserving collisions will be governed by the average of the A′ and A″ potentials, while the spin–orbit changing collisions will result from scattering on a surface determined by the difference between these two potentials.[15] No preferential population of the Λ-doublets is anticipated for pure case (a) scattering, and we did not attempt to resolve them in our experiments.

Nielson, Parker, and Pack calculated the A′ and A″ potentials in 1977 using the electron gas method.[23] The average potential is much larger than the difference potential, so the cross sections for multiplet conserving collisions are predicted to be much larger than those for the multiplet changing collisions. Joswig *et al.* measured state-resolved total cross sections for crossed-beam Ar–NO collisions using laser-induced fluorescence and indeed found roughly a factor of 10 difference in the cross sections.[21] Furthermore, they reported that the spin–orbit changing cross sections initially increased with $\Delta j$, in contrast to the trend normally exhibited in rotationally inelastic scattering. Recently, Gentry and co-workers have measured differential cross sections for Ar–NO in a crossed-beam experiment and also observe the increase in fine-structure changing cross section with final rotational level.[24] This behavior has also been observed in the multiplet changing collisions for NCO–He scattering,[19,22] and McDonald and Liu argue that it is a characteristic feature of

0022-3654/93/2097-6342$04.00/0 

inelastic scattering of case (a) molecules. Until recently,[12,24] state-resolved angular distributions had not been obtained for the inelastic scattering of a $^2\Pi$ molecule, and the results for the multiplet changing collisions presented here may provide useful insight into this aspect of such collisions.

Thuis and co-workers fit the integral cross-section data that they obtained from molecular beam scattering studies by expressing the average potential in terms of a Maitland–Smith (MS) anisotropic potential which contains a $P_1(\cos\theta)$ anisotropy term in the repulsion and a $P_2(\cos\theta)$ term in the repulsion and attraction.[25] The difference potential was neglected because of its very small magnitude compared to the average potential. The MS potential is accurate only within the probing range $1.5 < R/R_e < 2$, where $R$ is the distance between the colliding particles and $R_e$ is the position of the minimum in the isotropic potential. Casavecchia and co-workers determined the anisotropy of the Ar–NO potential from angular distributions obtained in a crossed-beam experiment at 0.079 and 0.095 eV.[26] They fit their results using a Morse–spline–van der Waals potential and found reasonable agreement with the conclusions of Thuis *et al.* The collision energies employed in our experiments (0.1, 0.18, and 0.35 eV) probe regions along the repulsive wall ($0.6 \leq R/R_e \leq 0.8$) and should complement the results of experiments probing other regions of the potential in refining the Ar–NO potential surface.[21,24-30]

Digital imaging techniques in combination with resonance-enhanced multiphoton ionization time-of-flight mass spectrometry (REMPI-TOF) were first used to obtain state-resolved angular distributions of the methyl radical from 355-nm photodissociation of methyl iodide.[11] Since the first report, the method has been vigorously applied to the study of unimolecular reactions (photodissociation)[31-34] and, in one instance, to the reactive scattering of H + HI, although in the latter case, only a single beam was used and angular distributions were not obtained.[35] A related technique has also been used in a beam–gas configuration, but without state-resolved detection.[36,37] An important difference between our apparatus and others currently in use in that the path from the collision region to the detector lies perpendicular to the plane of the beams, which cross at 90°. The nominal relative velocity vector thus always lies parallel to the plane of the image.

We have used the TOF ion imaging technique to study the following collision processes:

$$NO(^2\Pi_{1/2},v=0,j={}^1/_2) + Ar \rightarrow NO(^2\Pi_{1/2},v=0,j') + Ar \quad (I)$$

$$NO(^2\Pi_{1/2},v=0,j={}^1/_2) + Ar \rightarrow NO(^2\Pi_{3/2},v=0,j') + Ar \quad (II)$$

The results yield direct insight into the Ar–NO potential energy surface and shed some light on the nature of the spin–orbit changing collisions for these systems.

## II. Experimental Section

**A. General Description.** A schematic of the crossed-beam apparatus is shown in Figure 1. The Ar and NO source chambers are pumped by 6-in. diffusion pumps (Varian VHS-6). Typical background pressures in the source chambers when the valves are operating at the 10-Hz repetition rate of the experiment are $\sim 1 \times 10^{-4}$ Torr.

The interaction chamber is evacuated by a 4-in. diffusion pump (CVC) equipped with a water-cooled baffle and a liquid nitrogen trap. The background pressure in this chamber is $\sim 8 \times 10^{-8}$ Torr when both pulsed beams are operating. The differential pumping region for the NO beam is pumped by a 4-in. diffusion pump (CVC) which is also equipped with a water-cooled baffle, a liquid nitrogen trap, and an auxiliary 6-in. diffusion pump (Varian VHS-6). A chamber evacuated by a 6-in. diffusioin

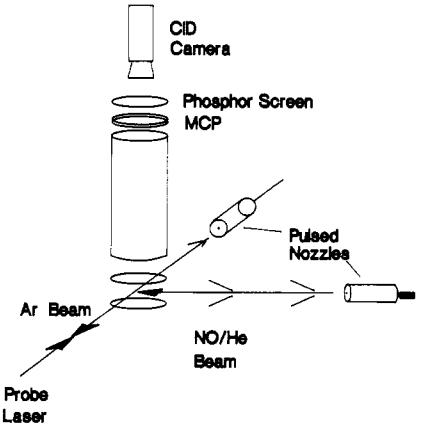


**Figure 1.** Schematic of the scattering apparatus.

pump (Varian VHS-6) is attached to the interaction chamber to serve as an NO beam dump. The two 6-in. diffusion pumps are necessary for reducing the background signal due both to NO molecules effusing from the differentially pumped region and to NO molecules from previous collisions that remain in the interaction region because of inefficient cryo-pumping of NO at liquid nitrogen temperatures. With the present configuration the data collection time is ~4 h (~100 000 laser shots) per rotational state for multiplet conserving collisions and 10–12 h for the spin–orbit changing collisions. The data collection is background-limited rather than signal-limited.

The pulsed molecular beam of NO is formed by expanding 7% NO in a carrier gas ($H_2$, He, or a mixture of He and Ne) at a total backing pressure of 1100 Torr through a nozzle (Precision Instruments) with a 0.5 mm diameter orifice. The NO beam is skimmed twice by 1 mm diameter skimmers (Beam Dynamics), collimating it into a diameter of less than 2 mm in the interaction region. The first skimmer is 3 cm from the front of the valve, and the second skimmer is 40 cm from the first skimmer. The beam travels another 40 cm to the center of the interaction chamber where it intersects the Ar beam at an angle of 90°. The pulsed Ar beam is formed by expanding 1040 Torr of pure Ar through a nozzle (Precision Instruments) which has a 0.3 mm diameter orifice and is located 15 cm from the interaction region. A 1 mm diameter skimmer (Beam Dynamics) collimates the Ar beam into a diameter of ~3 mm in the interaction region. The size of both beams in the interaction region can be directly measured by recording their ion images (in the case of the Ar beam this is done by seeding it with nitric oxide) as described later.

A pulsed laser with a wavelength near 226 nm is counter-propagated to the Ar beam to ionize a particular state of rotationally excited NO by (1+1) REMPI through the $A$ state. The tunable UV light is produced by mixing the fundamental of an injection seeded Nd:YAG laser (Quanta-Ray DCR-4) with the second harmonic of a dye laser (Quanta-Ray PDL2) operating with Rhodamine 610 (Exciton), which is itself pumped by the doubled output of the Nd:YAG laser. The UV light, typically 1–2 mJ pulse$^{-1}$ with a bandwidth of 0.35 cm$^{-1}$ (fwhm) and a 10-ns pulse duration, is sent through a telescope and a 120 cm focal length lens so that it is ~0.8 mm in diameter at the interaction region.

**B. Ion Detection.** An electric field of ~800 V cm$^{-1}$ is applied to extract the ions into a Wiley–Mclaren time-of-flight (TOF) mass spectrometer[38] whose flight axis is perpendicular to the plane defined by the molecular beams and the laser. The voltages used to bias the repeller and accelerator grids were chosen such that the ion cloud is flattened into a "pancake" shape just as it hits the first of a pair of microchannel plates (Galileo Electro-Optics Corporation), which together yield a gain of *ca.* $10^8$ electrons per ion.

The electrons are accelerated to a fast phosphor (P47, 80-ns

persistence time) coated onto one end of a fiber-optic bundle mounted through a flange in the vacuum chamber. The image is captured by a 512×480 pixel image-intensified CID camera (Xybion Electronic Systems ISG-204-DR-2). The intensifier is gated to the NO flight time. A video averager (Poynting Products RA-512) is used to sum 256 images in real time into a 512×480×16-bit buffer. An 8-bit slice (see below) of the resulting sum is normalized for laser power and stored in a 486 PC clone (Gateway 2000). The laser intensity is monitored by detecting the intensity reflected from an S1UV window placed in the laser beam path. The Ar beam is toggled on and off during the experiment, and the difference image is accumulated.

**C. Imaging Hardware.** A TN224MEG board (Epix) provides power (12 V) to the camera and converts the camera's non-interlaced 512×480 video output to a standard RS-170 video format which a high-resolution video board (Poynting Products 4MEGVID) can interpret and display. The TN224MEG board sends the video signal to the 4MEGVID board, which in turn sends it to the averager. The averaged images are then sent back to the 4MEGVID board and to the video monitor for display.

The RA-512 averager adds the 8-bit digital images provided by the 4MEGVID board into a 16-bit buffer. The number of images that can be averaged is given by $2^- = 2, 4, ..., 256$ where $N$ goes from 1 to 8. Since the 4MEGVID board can use only 8-bit images, the 16-bit averaged images must be converted to 8-bit images. Any 8-bit slice of the summed image may be selected, so the final image may represent an amplification of the original video.

The TN224MEG board serves as the master clock for the experiment. The board sends a 30-Hz signal to a homemade timing box where it is divided to produce a 10-Hz TTL signal. The 10-Hz signal is used to trigger a digital delay generator (Stanford Research Systems DG535) which controls the delays of the molecular beams, the laser, and the ion detection system. The laser is fired ~700 μs after the NO beam, and the repeller voltage is applied 10 ns before the laser pulse.

**D. Characterization of the Molecular Beams.** The rotational state distribution of the NO beam was determined by replacing the camera with a photomultiplier tube and setting the gate of a boxcar integrator (Stanford Research Systems SR250) to the NO mass peak while the ionization laser is scanned. A REMPI scan of the beam showed that the ratio of populations $N_{j=0.5}$: $N_{j=1.5}$:$N_{j=2.5}$ for the $^2\Pi_{1/2}$ electronic state is 1:0.037:0.006, corresponding to a rotational temperature <2.5 K. The population fraction in the $^2\Pi_{3/2}$ state was negligible.

By tuning the laser to ionize NO($^2\Pi_{1/2}$,$v$=0,$j$=0.5), the principal component of the beam, the imaging technique allows one to see the velocity distribution of the molecular beam and its spatial position and thus optimize overlap with the laser. The Ar beam velocity and position may similarly be obtained by seeding it with a trace of NO; the result agrees well with that expected for an isentropic expansion at 290 K. Speed ratios ($v/\Delta v$) for the Ar and NO beams are 8 and 12, respectively, resulting in a spread in the collision energy $\Delta E/E \approx 30\%$ full width at half-maximum.

The Newton diagram for the scattering process can be visualized readily and is shown in Figure 2. This figure is actually a superposition of two images. In one image, the laser propagates counter to the Ar beam (containing a trace of NO). We see a vertical strip corresponding to the laser beam propagating along the axis of the Ar/NO beam. A light spot to the left of the strip is also visible which corresponds to the He/NO beam. The spot is displaced because of the forward momentum of the NO in the beam. In the other image, the laser propagates counter to the He/NO beam and we see a horizontal strip (He/NO beam) and a light spot below the strip (NO seeded in Ar beam). The intersection of the two beams is the collision region. The light spots below and to the left of the intersection represent NO molecules that were ionized at the collision region and that moved a certain distance in the time between ionization and detection. Measurement of these distances and the delay time provides the beam velocities and, thus, also the collision energy. The dispersion and size for each molecular beam can be determined from the light spots. Precautions were taken to ensure that the images were not distorted by Coulomb explosion. Space–charge effects can be readily detected since the beams appear greatly expanded in the region of the laser focus if the laser power is too high.

**E. Angular Resolution.** The angular resolution of our apparatus is determined largely by the size of the scattering volume and the blurring that is introduced by collisions which occur before the laser fires. The angular resolution was estimated by simulating images from the machine parameters and a distribution with features of different angular widths. For $j' = 18.5$ at 0.18 eV, the images were not sensitive to features with width less than 8°. The angular resolution should be higher for the lower final rotational states at the same collision energy since the Newton spheres are larger. No attempt was made to optimize the angular resolution of our experiments since the broad features provided adequate information to gain insight into the potential energy surface.

## III. Simulation Program

The images obtained in these experiments are projections of the three-dimensional number density distributions onto the detector, so some means of extracting the differential cross sections, $I(\Theta)$, must be found. One approach, applicable whenever the three-dimensional distribution contains an axis of cylindrical symmetry parallel to the detection plane, is to perform an Abel transform of the recorded image.[39,40] This method, frequently used in the analysis of photodissociation experiments, has the virtue that the transformation is unique. It is extremely sensitive to noise, however, and it is difficult to deconvolute the effects of variations in detection efficiency.

Another approach, widely used in the analysis of crossed-beam experiments, is to perform an iterative convolution over the experimental parameters of assumed forms of the differential cross section. Forward convolution methods allow more accurate treatment of apparatus functions but do not yield a unique set of product distributions. Trial and error methods can be computationally expensive and may lack sensitivity to certain dynamical features. There exist two different means of performing this "forward convolution" analysis. The traditional method is to integrate the trial distributions directly over the apparatus functions to simulate the experimental results.[41-43] An alternative technique is to perform Monte Carlo simulations based on assumed forms of the distributions.[44,45] The latter approach has the advantage that integrable forms of machine parameters need not be found; the apparatus conditions may thus be treated rigorously. One may also use the simulations to explore the impact of different machine conditions, a procedure that can be very useful in optimizing the experimental configuration. The primary disadvantage of the Monte Carlo approach is the increased computational effort that is generally necessary for these calculations.

We have chosen to use the Monte Carlo based forward convolution analysis of these images because it allows for a rigorous treatment of many features of the experiment that would otherwise be difficult or impossible to treat accurately. These primarily result from the fact that the molecular beam pulses (~300 μs) are very much longer than the probe laser pulse (~10 ns) and the probe laser volume is considerably smaller than the interaction volume. These inequalities lead to an inhomogeneity in the detection efficiency; scattered particles possessing a small laboratory velocity perpendicular to the probe laser direction are detected more efficiently than those with higher laboratory velocities. In addition, much of the detected flux originates in scattering which occurs long (up to 3 μs) before the laser fires.

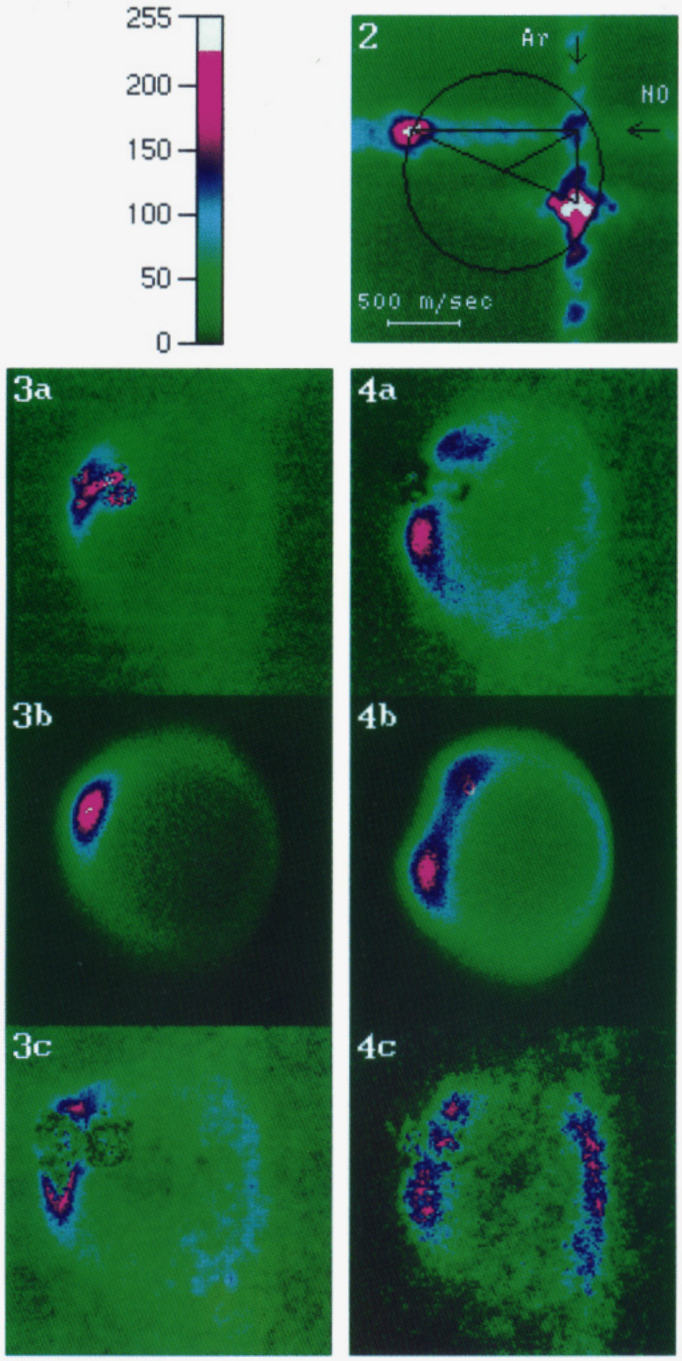


**Figure 2.** Newton diagram for Ar + NO scattering at 0.18 eV. The Newton circle for elastic scattering is superimposed. See text for details. **Figure 3.** Angular distributions for NO $j' = 7.5$ at 0.18 eV. Parts a and b are images obtained from experiment and simulation, respectively, for NO in the $^2\Pi_{1/2}$ state (multiplet conserving collision; $R_{21}$ line). Part c is the image obtained from experiment for NO in the $^2\Pi_{3/2}$ state (multiplet changing collision; $R_{22}$ line). **Figure 4.** Angular distributions for NO $j' = 11.5$ at 0.18 eV. Parts a and b are images obtained from experiment and simulation, respectively, for NO in the $^2\Pi_{1/2}$ state (multiplet conserving collision; $R_{11}$,$Q_{21}$ line). Part c is the image obtained from experiment for NO in the $^2\Pi_{3/2}$ state (multiplet changing collision; $Q_{22}$,$R_{12}$ line).

Such scattering results in some loss of angular resolution but little distortion. Fortunately, these apparatus functions can be readily treated in Monte Carlo simulations, and their effects are easily studied. There are other factors one must consider when analyzing these images: the flux to number density transformation, averaging over beam velocity distributions, projection of the three-dimensional distribution onto the two-dimensional detector, and the Doppler width of the probe laser. All of these factors are also readily incorporated into the simulation program. It is important to note that the usual laboratory to center-of-mass transformation Jacobian is unity in these imaging experiments.

The simulation program is loosely based on the "LabAvg" program developed by Continetti from codes originally written by Pack and Walker.[44] An initial guess for the differential cross sections is entered, along with molecular and laser beam characteristics and relevant machine dimensions. For each trajectory, a point in the scattering volume and a corresponding Newton diagram are randomly selected. Polar and azimuthal scattering angles are chosen for the trajectory, and the time relative to the laser pulse is also selected. Importance sampling is used wherever applicable. The laboratory velocity of the scattered particle is calculated, and the particle is allowed to propagate until the laser fires. If the scattered particle is in the probe laser volume at that time, it is detected; the components of its velocity in the detector plane are used to propagate it through the mass spectrometer to the detector, where these velocity components are subsequently binned. Since we are confident about the machine parameters (laser pulse width, beam velocities, *etc.*),

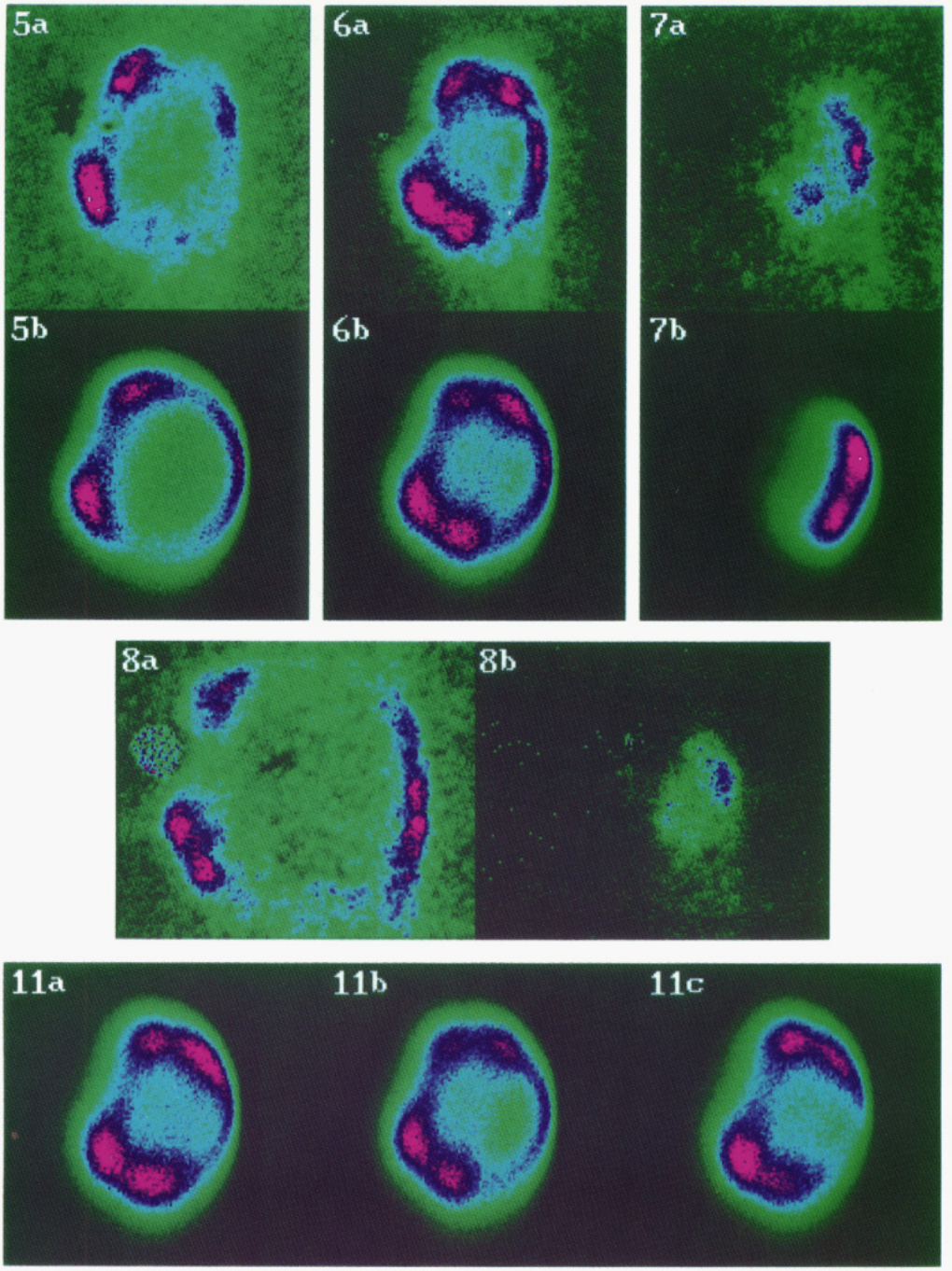


**Figure 5.** Angular distributions for NO($^2\Pi_{1/2}$,$j'$=14.5; $R_{11}$,$Q_{21}$ line) at 0.18 eV. Parts a and b are images obtained from experiment and simulation, respectively. **Figure 6.** Angular distributions for NO($^2\Pi_{1/2}$,$j'$=18.5; $Q_{11}$,$P_{21}$ line). Parts a and b are obtained from experiment and simulation, respectively, at 0.18 eV. **Figure 7.** Angular distributions for NO($^2\Pi_{1/2}$,$j'$=24.5; $Q_{11}$,$P_{21}$ line) at 0.18 eV). Parts a and b are images obtained from experiment and simulation, respectively. **Figure 8.** Angular distributions for NO($^2\Pi_{1/2}$,$j'$=18.5; $Q_{11}$,$P_{21}$ line) at 0.39 eV (a) and 0.11 eV (b). **Figure 11.** Images a, b, and c were obtained from the center-of-mass differential cross sections shown in Figure 10a–c, respectively.

the only free variable is the shape of the angular distribution function, and a good initial guess for this can be made by examining the extreme edge of the projected distribution. For scattered products with a single recoil energy, the intensities along the outer edge of the image would give the angular dependence of the differential cross section in the center-of-mass frame if the scattering volume were a point source and if the detection efficiency did not depend on velocity. Rough fitting can be accomplished using only $\sim 10^5$ trajectories (1–2 min on an IBM RS/6000) while the final simulations shown here were obtained with $10^7$ trajectories. The simulations which gave the minimum difference between the simulated and experimental images were considered to be the best fit to the data. As is the case with forward convolution methods involving a multidimensional parameter space, the determination of the error associated with each parameter is not trivial. To give the reader a sense of how sensitive the simulations are to variations of the differential cross sections, the Appendix shows the simulated images which are obtained from different forms of the differential cross sections for $j'$ = 18.5 at 0.18 eV.

## IV. Results

**A. Multiplet Conserving Collisions.** Results for the multiplet conserving collisions, process (I), are shown in Figures 3–7, along with the corresponding images generated by the simulation program. Images were obtained for final $j$ in the range 7.5–24.5; the maximum energetically allowed at the 0.18-eV collision energy appropriate for these figures is $j$ = $\sim$31.5. Specific rotational lines that were free of interference from overlapping lines were

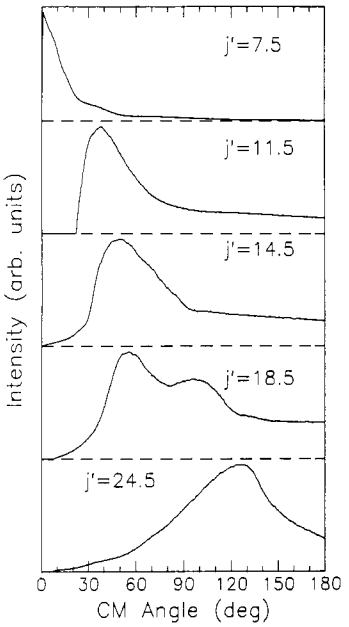


**Figure 9.** Best-fit center-of-mass differential cross sections for $NO(^2\Pi_{1/2}j')$ at 0.18 eV obtained from a Monte Carlo based simulation of the experimental images as described in section III.

chosen. The images were normalized independently but were not smoothed or filtered.

Several important aspects of the detection mentioned above are illustrated in these images. Because the pulse duration of the molecular beams is much longer than that of the probe laser, there is an increased sensitivity to products scattered with low velocities perpendicular to the probe laser direction. This results in an enhancement of the scattered signal along the laser axis. Since the relative velocity vector of the collision is not coincident with the propagation direction of the laser, the transitions have asymmetric line shapes. Because the line width of the laser (0.35 $cm^{-1}$) is not broad enough to sample the entire Doppler profile, the resulting images are not symmetric about the relative velocity vector. These effects are readily accounted for in the simulations. A final effect present in some of the images arises as a consequence of trace amounts of rotationally excited NO present in the beam. This background signal generally results in saturation of the video amplification in the vicinity of the beam itself, and we remove it if it is sufficiently far from the scattered distribution ($j' > 7.5$).

The most striking features of these distributions are the rotational rainbow peaks. These begin to appear at $j' = 11.5$ and move to more backward angles with increasing $\Delta j$. By $j' = 24.5$, the distribution is entirely backscattered. Another interesting aspect of the rainbow structure appears most clearly in the distributions for $j' = 18.5$. For this state, two separate rainbows may be seen to form the broad sideways scattered peak. A similar suggestion of this structure is present in the $j' = 14.5$ image.

All of the observations above are apparent in the differential cross sections obtained from the simulations (Figure 9). Although analysis allows us to be more quantitative, it is important to note the same observations may be made on the basis of the raw data alone. The essential features of the center-of-mass distributions are apparent in the original images. This is particularly so in the present case where the translational energy release is well-defined for each probed state, so that each distribution represents the projection of a single velocity sphere.

Images for $j' = 18.5$ were studied at three center-of-mass collision energies: 0.11, 0.18, and 0.39 eV, and these results are shown in Figures 6a and 8. At 0.11 eV, the $j' = 18.5$ state is near the maximum energetically allowed, and it appears entirely backscattered. At 0.18 eV, the double rainbows appear and the distribution is sideways scattered. At 0.39 eV, the distribution has moved entirely to the foward hemisphere and a suggestion of the double rainbow remains.

**TABLE I: $A - B$ for the Ar–NO System Calculated from a 2-D Hard Ellipse Model**

| $j'$ | $\theta_r$ (deg) | $\theta_{r,cl}$ (deg) | $J/p_0$ (Å) | $A-B$ (Å) | avg $A-B$ (Å) | ref |
|---|---|---|---|---|---|---|
| 11.5 | 40 | 60 | 0.300 | 0.300 | 0.32 | this work |
| 14.5 | 50 | 75 | 0.379 | 0.311 | 0.37 | 23 |
| 18.5 | 60 | 85 | 0.483 | 0.357 | 0.39 | 25 |
| 24.5 | 135 | 150 | 0.640 | 0.331 | 0.24 | 26 |

**B. Multiplet Changing Collisions.** Images corresponding to process (II) were studied for $j' = 7.5$ and 11.5 at 0.18 eV. The results are shown in Figures 3 and 4, along with the corresponding images for process (I) to facilitate comparison. The signal intensity was much lower for these channels, so longer accumulation times were necessary (*ca.* 12 h) and increased noise is present in these images. Nevertheless, the most striking feature of these distributions is the general similarity between the process (I) and process (II) distributions for a given final $j'$. Although there appears to be more backscattered signal in the process (II) images, the relative contribution that it makes to the overall signal cannot be accurately determined due to the low signal-to-noise ratio in these images.

## V. Discussion

**A. Multiplet Conserving Collisions.** Rotational rainbow peaks in atom–diatom inelastic scattering were first seen in TOF spectra from crossed-beam K–$N_2$ and K–CO experiments.[46,47] Although individual rotational states were not resolved in the original experiments, it was immediately recognized that the effect bore some analogies to the elastic scattering rainbows well-known from atom–atom scattering. Thomas, Beck, and others showed that this phenomenon arose from the anisotropy of the repulsive atom–diatom potential and was anticipated at the level of classical scattering from a hard ellipsoid.[47,48] Korsch and Schinke showed the detailed origin of these rainbow peaks in singularities in the mapping from $(L,\gamma)$ to $(\Theta,j)$, where $L$ is the orbital angular momentum, $\gamma$ the orientation angle of the ellipsoid, $\theta$ the scattering angle, and $j$ the final rotational state.[49] Schinke and Bowman showed that the rotational rainbow phenomenon is equivalently revealed in the angular distributions for specific final $j$ states, or in the rotational distributions at fixed laboratory scattering angles.[50]

The data for the multiplet conserving collisions shown in Figures 3–7a and summarized in Figure 9 display the trends characteristic of rotational rainbow distributions. For low $\Delta j$, the distributions are strongly forward scattered and no rainbow peak is apparent. When the rotational excitation is significant, however, the distribution rises sharply from near zero in the classically forbidden forward direction to the rainbow peak. It then declines more slowly at the larger scattering angles. Although supernumerary rainbows have been observed in some homonuclear scattering,[4] none are apparent in these distributions.

Beck and co-workers sought to relate features of their TOF distributions to attributes of the potential energy surfaces using a three-dimensional hard ellipsoid model.[47,46] Shortly afterwards, Bosanac developed a useful two-dimensional model that allows one to relate the rainbow positions directly to the difference between the semiaxes of a hard ellipse potential:[51]

$$A - B = \frac{J}{p_0}\left(2\sin\left(\frac{\theta_{r,cl}}{2}\right)\right)^{-1} \quad (1)$$

where $J$ is the rotational angular momentum, $p_0$ is the initial linear momentum, $\theta_{r,cl}$ is the classical rainbow position, and $A$ and $B$ are the semimajor and semiminor axes of the ellipse, respectively. The classical rainbow positions are found to occur somewhat behind the quantum mechanical and experimental

rainbow positions and are estimated as the point at which the distributions have fallen to 44% of the peak value.[49] Table I shows the experimental, $\theta_r$, and classical rainbow, $\theta_{r,cl}$, positions along with the $A - B$ values obtained using (1). The data yield an average for $A - B$ of 0.32 Å, which compares reasonably well with the value 0.37 Å that we obtain from a fit to the sum potential obtained from the electron gas model at this collision energy (0.18 eV). We also estimated average $A - B$ values of 0.39 and 0.24 Å from the anisotropic potentials of Thuis *et al.* and Casavecchia *et al.*, respectively.

The above analysis is strictly appropriate for homonuclear molecules. For heteronuclear molecules two rainbows are expected, corresponding to scattering involving the two different ends of the molecule. They are most clearly evident in the images for $j' = 14.5$ and 18.5 (Figures 5 and 6). Although anticipated for heteronuclear scattering, these double rainbows have not previously been directly observed in the angular distributions. Beck *et al.* saw an additional feature in their TOF spectra for K–CO scattering compared to K–$N_2$, and this feature was found to shift with isotopic substitution.[47] This additional peak corresponds to a secondary maximum in the $j'$ distributions, again a manifestation of the same phenomenon in the $j$ representation rather than the $\theta$ representation.

Bosanac and Buck extended the two-dimensional hard ellipse model to accommodate heteronuclear molecules and obtained a relation between the location of the two rainbow peaks and the eccentricity of the ellipse, *i.e.*, the shift, $\delta$, between the center of symmetry of the potential and the center of mass of the molecule.[52] In the two-dimensional picture, the rainbow occurs at the maximum effective impact parameter for a given $\Delta j$. In this model, the maximum effective impact parameter, $b_n$, may be inferred from the rainbow positions:

$$b_n = \frac{J}{p_0}\left[2\sin\left(\frac{\theta_{r,cl}}{2}\right)\right]^{-1}\left[1 - \epsilon\left(\frac{J}{p_0}\right)^2\right]^{-1/4} \qquad (2)$$

where the anisotropy parameter, $\epsilon$, is given by the ratio of the reduced mass of the system to the moment of inertia of the ellipse:

$$\epsilon = \mu/I$$

Two rainbows appear in scattering of heteronuclear molecules because there are two different $b_n$ which yield the same $\Delta j$, corresponding to the two different ends of the molecule. This interpretation was also explicit in the original three-dimensional treatment of Beck *et al.*[46,47] The difference in the effective impact parameters may be used to derive the eccentricity of the potential, $\delta$, if the scale of the ellipse is known:

$$\delta = \left(\frac{b_{n_1} - b_{n_2}}{2}\right)\left(\frac{A+B}{A}\right)^{1/2} \approx \frac{b_{n_1} - b_{n_2}}{(2)^{1/2}\left(1 + \frac{A-B}{4A}\right)} \qquad (3)$$

Using the value of the semimajor axis of the ellipse obtained from the potential of Nielson, Parker, and Pack and our $A - B$ value, we find $\delta = 0.06$ Å. This agrees reasonably well with the estimate obtained by inspection of the *ab initio* potential, 0.10 Å, and provides some assurance that the eccentricity of the potential is indeed responsible for the double rainbow peaks. The modified Maitland–Smith potential of Thuis *et al.* gives $\delta = 0.022$ Å, although this might be meaningless because the fit has little sensitivity in the region probed at 0.18 eV. Rainbows recently observed in oriented NO surface scattering provide an interesting alternative view of the eccentricity of the NO charge cloud.[53] In these experiments, oriented NO molecules selected by means of hexapole focusing were scattered off a Ag(111) surface and state-resolved angular distributions measured. The rotational rainbow appearing at high $j$ ($j = 23.5$) could be assigned unambiguously to scattering off of the O-atom end of the molecule. The N-end rainbow was not as clear under a dominant Boltzmann-like distribution, but a feature at $j = 8.5$ appeared as a likely candidate. This is consistent with the simple hard ellipse picture above: the low $j$ (or smaller angle) rainbow corresponds to scattering involving the lighter end of the molecule.

The energy dependence of the angular distributions observed for $j' = 18.5$ is consistent with predictions based on simple models. The rainbows move forward with increasing collision energy. This may not be a direct consequence of accessing different regions of the potential, however. From a classical perspective, it may be viewed as a result of reduced collision time owing to the increased relative velocity. When the collision duration decreases, the momentum transfer is less efficient, and smaller deflection angles accompany the trajectories. These trends have been observed previously in other systems.[3] The NO surface scattering experiments showed a somewhat different energy dependence. The rainbow corresponding to the O-end of the molecule, at fixed scattering angle, moved to higher $j$ with increasing collision energy.[53] This is analogous to the decrease in scattering angle, for fixed $j$, that we observe. While we see both rainbows moving together, the N-end distribution in the surface experiments is relatively insensitive to translational energy. This is likely the consequence of complex interactions with the surface, such as multiple collisions and trapping, which contribute to the low $j$ distributions.

**B. Multiplet Changing Collisions.** The mechanism responsible for the multiplet changing collisions is an intriguing puzzle. Arthurs and Dalgarno introduced the theoretical approach to rotationally inelastic scattering of diatomic molecules that has generally been employed by successive workers in the field.[54] Klar extended their ideas to treat molecules in $\Pi$ states,[13] and Green and Zare followed with a detailed theory for collision-induced transitions between $\Lambda$-doublets in $^1\Pi$ molecules.[55] The latter authors showed that although the collision involves two potential energy surfaces correlating to the two $\Lambda$-doublets of the molecule, the collision may be viewed as occurring on a single surface that in turn depends on the angle of rotation about the internuclear axis of the diatomic molecule. Shapiro and Kaplan extended these ideas to treat collisions of H with OH($^2\Pi$), the first detailed treatment of rotationally inelastic scattering of $^2\Pi$ molecules. Alexander generalized these ideas to include coupled states and infinite-order sudden approximations for open-shell systems with particlar emphasis on the NO–Ar system.

Alexander pointed out a propensity rule governing collisions of $^2\Pi$ molecules with structureless targets: for large values of the total angular momentum, transitions that preserve the parity index are strongly favored.[15] Alexander also made explicit an assertion of Nielson *et al.*, that multiplet changing collisions for case (a) molecules are induced by the difference potential, $V^-$, while multiplet conserving collisions are mediated by the average potential, $V^+$.[16] Because these two potentials are so different, it is surprising that the angular distributions for the multiplet conserving and multiplet changing collisions shown in Figures 3 and 4 are so similar. In fact, these angular distributions alone strongly suggest that direct coupling via the difference potential is not the primary pathway for multiplet changing collisions, at least for these states.

The previous results of Joswig *et al.*[21] for the multiplet changing collision at 0.05 eV contain several interesting features that indicate that the rotational excitation does not proceed in the same manner as RET within a single electronic manifold. The experimental cross sections for scattering out of the ground rotational state were found to *increase* with increasing final rotational level up to some intermediate value before falling at large values of $j'$. This behavior is in complete contrast to RET in, for example, $^1\Sigma$ states, where the probability for energy transfer is found to fall almost exponentially with $\Delta j$.[56] The coupled states calculations of Orlikowski and Alexander reproduced this

behavior, but its origin was not clear.[16] The *ab initio* potential is not thought to be very accurate, however, and Nielson and co-workers particularly warned against ascribing too much significance to calculations based on their difference potential. Nevertheless, these results are puzzling. Orlikowski and Alexander suggested that since the difference potential is so weak for this system, the multiplet changing collisions might actually take place via "virtual transitions involving the stronger coupling within the $\Omega = {}^1/_2$ and $\Omega = {}^3/_2$ manifolds."[16]

In a closely related experiment, McDonald and Liu measured state-resolved integral cross sections for NCO–He inelastic scattering.[19,22] NCO is a linear $^2\Pi$ radical, also well-described in Hund's case (a) ($A/B = -245$). Here, too, the multiplet changing collisions show a bell-shaped $j'$ distribution, and the authors suggest that such a distribution will be a characteristic feature for multiplet changing collisions in case (a) molecules. McDonald and Liu also invoked an "indirect process" ($\Omega = {}^1/_2 j' \rightarrow \Omega = {}^1/_2 j'' \rightarrow \Omega = {}^3/_2 j''$) to account for this effect, and they underline the importance of the coupling of nuclear motion with the electronic degrees of freedom by use of the phrase "dynamical Renner–Teller effect" to describe this phenomenon.

Our results suggest the importance of the average potential for both fine structure conserving and fine structure changing collisions, since the angular distributions are so similar. But what is the precise nature of the coupling that is responsible for the electronic transition? McDonald and Liu again invoke the difference potential and argue that the low impact parameter collisions, which lead to enhanced rotational excitation, penetrate to shorter range where the difference potential may be significant.

We suggest an alternative mechanism to account for the fine structure changing collisions. The assertion that multiplet changing collisions are governed by the difference potential is strictly valid within Hund's case (a). Although Shapiro and Kaplan studied H + OH($^2\Pi$), a spin 1, case (b) system, their analysis is relevant to Ar–NO in the intermediate coupling case.[14] These authors point out that the operator $\Omega$ does not commute with the total Hamiltonian since the nuclear rotational Hamiltonian couples the nuclear and electronic motions. They write the total diatom rotor Hamiltonian as a sum of the zero-order Born–Oppenheimer electronic Hamiltonian with an additional component, $H_1$, containing the spin–orbit and nuclear rotation operators which serve to couple the Born–Oppenheimer eigenstates:

$$H = H_0^{el} + H_1 \tag{4}$$

$H_1$ may be written as a sum of terms which are diagonal and off-diagonal in $\Lambda$. The diagonal component is of interest to us:

$$H_1^{dia} = B[J(J+1) + S(S+1) - \Omega^2 - \Sigma^2] + A\Lambda\Sigma + B[L_x^2 + L_y^2 - J_+S_- - J_-S_+] \tag{5}$$

The last term of the preceding equation contains the spin–rotation coupling, which can also induce transitions between the different spin–orbit states. Shapiro and Kaplan point out that these nuclear–electronic coupling terms are negligible in relation to the interaction potential when the system approaches the collision region. This "non-Born–Oppenheimer" coupling serves only to determine the product state distribution; the mixing occurs in the asymptotic region. The magnitude of this coupling is proportional to the rotational constant, and to $J$, the total rotor angular momentum. Alexander also noted that the J·S term in the molecular Hamiltonian mixes to the two fine structure states, and this mixing will increase with increasing $j$. The coupled states calculations naturally incorporate this contribution.[16]

This interpretation is consistent with the trends shown in the multiplet changing collisions: the cross sections rise linearly with $j$, independent of collision energy. The latter point is particularly difficult to rationalize in terms of the difference potential. For large values of $j$, this spin–rotation coupling may become quite efficient, and the cross sections for the multiplet changing collisions might approach those of the multiplet conserving collisions, as observed experimentally. The question thus becomes one of ascertaining which effect is dominant: if the difference potential is quite small, then the non-Born–Oppenheimer contribution may prevail. This may be the more general case for scattering of Hund's case (a) molecules. It would be interesting to examine the importance of this spin–rotation coupling by suppressing it in the calculations.

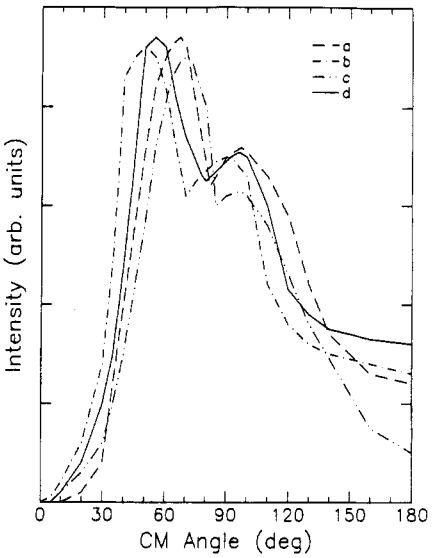


**Figure 10.** Assumed forms of the center-of-mass differential cross sectioins for NO($^2\Pi_{1/2}j'$=18.5; $Q_{11}$,$P_{21}$ line). Plots a, b, and c were used as input into the simulations that generated the images in Figure 11. Plot d was used as input into the simulation that generated the best fit (Figure 6b) to the experimental image (Figure 6a).

## VI. Conclusion

We have obtained state-to-state differential cross sections for inelastic collisions of NO with Ar in a crossed-beam experiment. Rotational rainbow peaks appear in the angular distributions, and these move to backward scattering angles with increasing $j'$. The images are analyzed using a Monte Carlo based forward convolution program that accounts for the transformation from the center-of-mass differential cross sections to the experimental image. The rainbow positions are analyzed using a simple two-dimensional hard ellipse model to provide quantitative insight into the anisotropy of the potential energy surface: a value of 0.32 Å was obtained for the difference between the semimajor and semiminor axes. For NO ($j'$ = 18.5), two rainbow peaks are observed. These double rainbows are predicted for heteronuclear molecules but have not previously been directly observed in the angular distributions. The 2-D analysis is used to obtain the eccentricity of the hard ellipse potential from the positions of the two rainbow peaks. At 0.18 eV collision energy, a value of 0.06 Å was obtained for $\delta$, the eccentricity of the ellipse. Finally, the angular distributions for the spin–orbit conserving collisions and spin–orbit changing collisions are remarkably similar, though they were thought to involve two different potential energy surfaces. An alternative mechanism is proposed to account for the spin–orbit changing collisions through non-Born–Oppenheimer–rotation coupling.

The experiment represents an extension of the ion-imaging technique to a genuine crossed-beam configuration. This new experimental method is general and versatile: it may be used wherever REMPI techniques are applicable, and quantum state resolved angular distributions are obtained for all scattering angles simultaneously.

**Acknowledgment.** We are grateful for support of this work to the U.S. Army Research Office under Grant No. DAAL03-91-

G-0125 and to the Department of Energy under Grant No. DEFG02-88ER13934. We would like to acknowledge the MRL Program of the National Science Foundation under Award No. DMR-9121654 for supplying the IBM RS/6000 used for image analysis. We are also grateful to the Science and Engineering Research Council for the award of an Advanced Research Fellowship to B.J.W. and to NATO for the award of a colloborative travel grant to B.J.W. and P.L.H. We would like to thank Dr. V. Hradil, Professor S. A. Hewitt, and Dr. T. Suzuki for help in the initial stages of the experiment, Dr. F. Suits for valuable suggestions on image acquisition, and the MSC computing staff (R. Cochran, L. Smith, and D. Svitavsky) for excellent technical support. A.G.S. and B.J.W. would also like to thank Professor M. H. Alexander for discussions on spin–orbit changing collisions. We would like to dedicate this work to the memory of Miles Davis.

## Appendix

To illustrate qualitatively the sensitivity of the simulations to small variations in the input differential cross sections, Figures 10 and 11 show different forms of the differential cross sections and the corresponding images generated by the simulations for $j' = 18.5$ at 0.18 eV.

## References and Notes

(1) Lee, Y. T. *Science* **1987**, *236*, 793.
(2) Parson, J. M.; Schafer, T. P.; Tully, F. P.; Siska, P. E.; Wong, Y. C.; Lee, Y. T. *J. Chem. Phys.* **1967**, *46*, 3693.
(3) Bergmann, K.; Engelhardt, R.; Hefter, U.; Hering, P.; Witt, J. *Phys. Rev. Lett.* **1978**, *40*, 1446.
(4) Jones, P. L.; Hefter, U.; Mattheus, A.; Witt, J.; Bergmann, K.; Mueller, W.; Meyer, W.; Schinke, R. *Phys. Rev. A* **1982**, *26*, 1283.
(5) Faubel, M.; Kohl, K.-H.; Toennies, J. P.; Tang, K. T.; Yung, Y. Y. *Faraday Discuss. Chem. Soc.* **1982**, No. 73, 205.
(6) Buck, U. *Faraday Discuss. Chem. Soc.* **1982**, No. 73, 187.
(7) Suits, A. G.; de Pujo, P.; Sublemontier, O.; Visticot, J.-P.; Berlande, J.; Cuvellier, J.; Gustavsson, T.; Mestdagh, J.-M.; Meynadier, P.; Lee, Y. T. *Phys. Rev. Lett.* **1991**, *67*, 3070.
(8) Gentry, W. R.; Giese, C. F. *Phys. Rev. Lett.* **1977**, *39*, 1259.
(9) Girard, B.; Billy, N.; Gouedard, G.; Vigue, F. *Europhysics Lett.* **1991**, *14*, 13.
(10) Murphy, E. L.; Brophy, J. H.; Arnold, G. S.; Dimpfl, W. L.; Kinsey, J. L. *J. Chem. Phys.* **1979**, *70*, 5910.
(11) Chandler, D. W.; Houston, P. L. *J. Chem. Phys.* **1987**, *87*, 1445.
(12) Suits, A. G.; Bontuyan, L. S.; Houston, P. L.; Whitaker, B. J. *J. Chem. Phys.* **1992**, *96*, 8618.
(13) Klar, H. *J. Phys. B* **1973**, *6*, 2139.
(14) Shapiro, M.; Kaplan, H. *J. Chem. Phys.* **1978**, *71*, 2182.
(15) Alexander, M. H. *J. Chem. Phys.* **1982**, *76*, 5974.
(16) Orlikowski, T.; Alexander, M. H. *J. Chem. Phys.* **1983**, *79*, 6006.
(17) Alexander, M. H. *Chem. Phys.* **1985**, *92*, 337.
(18) Sonnenfroh, D. M.; McDonald, R. G.; Liu, K. *J. Chem. Phys.* **1991**, *94*, 6508.
(19) McDonald, R. G.; Liu, K. *J. Phys. Chem.* **1991**, *95*, 9630.
(20) Cohen, S. R.; Naaman, R.; Balint-Kurti, G. G. *Chem. Phys.* **1989**, *134*, 119.
(21) Joswig, H.; Andresen, P.; Schinke, R. *J. Chem. Phys.* **1986**, *85*, 1904.
(22) McDonald, R. G.; Liu, K. *J. Chem. Phys.* **1992**, *97*, 978.
(23) Nielson, G. C.; Parker, G. A.; Pack, R. T. *J. Chem. Phys.* **1977**, *66*, 1396.
(24) Jons, S. D.; Shirley, J. E.; Vonk, M. T.; Giese, C. F.; Gentry, W. R. *J. Chem. Phys.* **1992**, *97*, 7831.
(25) Thuis, H. H. W.; Stolte, S.; Reuss, J.; Van Den Biesen, J. J. H.; Van Den Meijdenberg, C. J. N. *Chem. Phys.* **1980**, *52*, 211.
(26) Casavecchia, P.; Laganà, A.; Volpi, G. G. *Chem. Phys.* **1984**, *112*, 445.
(27) Sato, K.; Achiba, Y.; Kimura, K. *J. Chem. Phys.* **1984**, *81*, 57.
(28) Mills, P. D. A.; Western, C. M.; Howard, B. J. *J. Phys. Chem.* **1986**, *90*, 4961.
(29) Niemann, J.; Naaman, R. *J. Chem. Phys.* **1986**, *84*, 3825.
(30) Miller, J. C. *J. Chem. Phys.* **1989**, *90*, 4031.
(31) Chandler, D. W.; Janssen, M. H. M.; Stolte, S.; Strickland, R. N.; Thoman, J. W., Jr.; Parker, D. H. *J. Phys. Chem.* **1990**, *94*, 4839.
(32) Thoman, J. W.; Chandler, D. W.; Parker, D. H.; Janssen, M. H. M. *Laser Chem.* **1988**, *9*, 27.
(33) Baldwin, D. P.; Buntine, M. A.; Chandler, D. W. *J. Chem. Phys.* **1990**, *93*, 6578.
(34) Suzuki, T.; Hradil, V. P.; Hewitt, S. A.; Houston, P. L.; Whitaker, B. J. *Chem. Phys. Lett.* **1991**, *187*, 257.
(35) Buntine, M. A.; Baldwin, D. P.; Zare, R. N.; Chandler, D. W. *J. Chem. Phys.* **1991**, *94*, 4672.
(36) Kalamarides, A.; Marawar, R. W.; Durham, M. A.; Lindsay, B. G.; Smith, K. A.; Dunning, F. B. *J. Chem. Phys.* **1990**, *93*, 4043.
(37) Ling, X.; Durham, M. A.; Kalamarides, A.; Marawar, R. W.; Lindsay, B. G.; Smith, K. A.; Dunning, F. B. *J. Chem. Phys.* **1990**, *93*, 8669.
(38) Wiley, W. C.; Mclaren, I. H. *Rev. Sci. Instrum.* **1955**, *26*, 1150.
(39) Strickland, R. N.; Chandler, D. W. *Appl. Opt.* **1991**, *30*, 1811.
(40) Castleman, K. R. *Digital Image Processing*; Prentice Hall: Englewood Cliffs, NJ, 1979.
(41) Entemann, E.; Herschbach, D. *J. Chem. Phys.* **1971**, *55*, 4872.
(42) Buss, R. Ph.D. Thesis, University of California, Berkeley, 1972.
(43) Pack, R. T. *J. Chem. Phys.* **1984**, *81*, 1841.
(44) Continetti, R. E. Ph.D. Thesis, University of California, Berkeley, 1989.
(45) Continetti, R. E.; Balko, B. A.; Lee, Y. T. *J. Chem. Phys.* **1990**, *93*, 5719.
(46) Schepper, W.; Ross, U.; Beck, D. *Z. Phys. A* **1979**, *290*, 131.
(47) Beck, D.; Ross, U.; Schepper, W. *Phys. Rev. A* **1979**, *19*, 2173.
(48) Thomas, L. D. *J. Chem. Phys.* **1977**, *67*, 5224.
(49) Korsch, H. J.; Schinke, R. *J. Chem. Phys.* **1981**, *75*, 3850.
(50) Schinke, R.; Bowman, J. M. *Molecular Collision Dynamics*; Bowman, J. M., Ed.; Springer-Verlag: Berlin, 1983.
(51) Bosanac, S. *Phys. Rev. A* **1980**, *22*, 2617.
(52) Bosanac, S.; Buck, U. *Chem. Phys. Lett.* **1981**, *81*, 315.
(53) Geuzebroek, F.; Wiskerke, A. E.; Tenner, M. G.; Kleyn, A. W.; Stolte, S.; Namiki, A. *J. Phys. Chem.* **1991**, *95*, 8409.
(54) Arthurs, A. M.; Dalgarno, A. *Proc. R. Soc. London Ser. A* **1960**, *256*, 540.
(55) Green, S.; Zare, R. N. *Chem. Phys.* **1975**, *7*, 62.
(56) McCaffery, A. J.; Proctor, M. J.; Whitaker, B. J. *Annu. Rev. Phys. Chem.* **1986**, *37*, 223.